The toughness of porcine skin: Quantitative measurements and microstructural characterization

Andrei Pissarenko [a], Wen Yang [a,b], Haocheng Quan [a], Boris Poyer [c], Alun Williams [d],
Katherine A. Brown [d,e], Marc A. Meyers [a,*]

[a] University of California, San Diego, CA, USA
[b] Lawrence Berkeley National Laboratory, Berkeley, CA, USA
[c] École Normale Supérieure de Paris-Saclay, Cachan, France
[d] University of Cambridge, Cambridge, UK
[e] University of Texas Austin, Austin, TX, USA

ABSTRACT

An exceptional tear resistance is required of the skin to protect the body from external attacks, environmental damage, and other forms of aggression. To estimate the toughness of juvenile porcine skin, we conduct two types of experiments on pre-notched specimens, placing the tissue under shear (Mode III) by using the classical trouser test with a 25 mm long pre-notch, and opening (Mode I) with an experimental setup with the same pre-notch length. We obtain two distinct average toughness values of $J_{IIIc} \approx 20.4 kJ/m^2$ and $J_{Ic} = 30.4 kJ/m^2$, as a result of differences between these two modes of crack-tip loading and propagation, and collagen alignment. Digital image correlation coupled with single edge notch tests of 10 mm $\times$ 30 mm skin samples enables the mapping of the local strains around the tip of the crack. Effects of sample orientation and initial notch size ratio on the strain profile and on the net-section failure stress are discussed. The evaluation of the structure at the crack tip and regions undergoing more uniform states of deformation is conducted by *ex situ* transmission electron microscopy and *in situ* environmental scanning electron microscopy. Prior to crack propagation, the stress concentration is decreased by redistributing loads away from the crack tip, illustrated by gradual recruitment of collagen fibers ahead of the crack tip, thus delaying crack growth. After the crack has propagated, collagen fibers are substantially damaged, marked by delamination and recoil of the collagen fibrils.

1. Introduction

As the outermost layer of the body, and consequently the first protective barrier against external aggression, it is important for the skin to maintain its structural integrity throughout life. Injuries can result in tears or scratches that easily become sites with an increased risk of infection. Moreover, it is crucial that these damaged areas do not expand or grow to a critical extent following movement, which would considerably affect the efficiency of the healing process. Surgical interventions often require that external tissues be incised, in order to facilitate access to the regions to treat. Considerable efforts have been made to reduce the size of incisions, for cosmetic purposes, but also to minimize exposure and the formation of scar tissue. Repeated access through the area of intervention generates load concentration around the incised region, potentially causing tear propagation. In skin, this process is mitigated

thanks to its remarkable resistance to tearing, a property that has recently been characterized by Yang et al. (2015) for rabbit. Fibers in the dermis realign in the direction of tension and help alleviate the stresses which concentrate around the tear. This process of realignment was observed and quantified by small angle X-ray scattering (SAXS) and can be seen macroscopically as the region around the tear starts to blunt, replacing sharp crack tips which are regions of stress concentration. This process was also evidenced for thinner collagenous tissues using multi-photon imaging (Bircher et al., 2019). Nonetheless, although some light has been shed on the mechanisms at stake during tear propagation, quantitative information on the toughness of skin is incomplete. Such knowledge is of considerable interest in designing better strategies for surgical pre-planning, or minimizing scar tissue formation by improving healing techniques.

Wegst and Ashby (2004) compiled modulus-toughness plot for the

---

principal biological materials, including skin. The measure used for toughness is J_c, corresponding to the energy required to create a new crack area per unit surface in a given material. The Wegst-Ashby plot reports that skin exhibits amongst the highest values of J_c with a rather low elastic modulus. According to a criterion where the material must support a given displacement without failure, reflected by the parameter (diagonal in plot) $M_{12} = (J_c/E)^{1/2}$, skin performs particularly well. It is interesting to observe that in an earlier publication, Ashby et al. (1995) had a plot with a much wider range in moduli and in toughness for skin, namely $E \approx 2 \cdot 10^{-3} - 1.5 \cdot 10^{-1} GPa$ and $J_c \approx 1 - 20 kJ/m^2$, while the updated plot shows $E \approx 0.01 - 0.07\ GPa$ and $J_c \approx 6 - 30 GPa$, suggesting that our understanding of these measures is becoming more accurate. The compiled values come from tests conducted on different species, for which the variation can be quite broad (Pissarenko and Meyers, 2019), and from different methods used to measure a given material property, influencing the final result. Since skin is a nonlinear elastic material, the estimation of a single modulus of elasticity is also questionable (Rodrigues, 2001). For toughness, it appears that the results by Bauer et al. (1989) on lizard skin, Purslow (1989) on rat skin, and Vincent (1990) on rabbit skin were used as a reference in the Wegst-Ashby plots. The methods for the estimation of toughness differed: Bauer et al. (1989) calculated the area under the stress-strain curve, while Purslow (1989) used the trouser test. It is likely that the results on lizard skin were ultimately removed in the latest versions of the Ashby plots (Wegst and Ashby, 2004). The data used to estimate the toughness of skin are therefore rather limited and suffer from large variations due to the influence of species and of the testing method.

More recently, Comley and Fleck (2010) calculated a toughness of $J_c = 17 \pm 4\ kJ/m^2$ for pig skin from trouser tests, which is in good agreement with the previously mentioned range. Note that for trouser tests, the pulling direction is out-of-plane, implying that the fracture occurs in Mode III. The calculated toughness thus corresponds to this specific shear mode, which is not necessarily the principal mode of tear propagation in skin.

In-plane tension, which has been studied extensively over the past few years (Ankersen et al., 1999; Ní Annaidh et al., 2012; Ottenio et al., 2015; Pissarenko et al., 2019; Yang et al., 2015), is probably the principal mode of deformation in skin. On the other hand, for the study of toughness, conventional in-plane methods can be limited by the fact that it is difficult to maintain a skin sample flat during the test. This difficulty can be overcome in shear tests. For pure shear, where the width has to be 6 to 10 times larger than the gage length (Rivlin and Thomas, 1953), the area to grip becomes considerably large and can become problematic. Hollenstein et al. (2011) proposed a solution by taking thin slices of the dermis using a dermatome. This offers interesting perspectives for the testing of tear propagation in such conditions, although whether properties obtained for a thin slice can be transferred to the properties of a full section of skin could be problematic.

In a recent study on the toughness of arapaima scales (Yang et al., 2019), an experimental setup was developed to conduct crack opening tests (mode I). The sample geometry is quite similar to the one for trouser tests, except that both legs are pulled apart from each other along the surface plane. The grips are free to rotate in the out-of-plane direction, facilitating the opening motion. Plexiglass sheets are used to confine the unstretched portion of the sample, preventing it from folding or buckling. This is particularly important for the testing of thin biological materials and soft tissues.

Other possible in-plane methods are the single edge notch tension (SENT) and the centrally cracked tension (CCT) tests. In each case, a tensile specimen is notched perpendicularly to the tensile direction with a sharp cut at mid-length, either on one side of the sample (SENT), or symmetrically in its center (CCT). CCT tests can be preferred for the symmetry of the sample and of the loading conditions, allowing for an easier observation of the tear ovalization in the case of skin (Yang et al., 2015), while SENT tests are more favorable if one wants to focus on the

process of tear propagation, since it will initiate along the notch. While this method is well implemented in the context of linear elastic fracture mechanics (LEFM), or elastic-plastic fracture mechanics, several assumptions on the mechanical behavior of the tissue as well as on the local stress distribution around the crack are necessary to analytically determine the toughness of soft tissues.

The use of digital image correlation (DIC) to measure the local deformation of skin during stretching has gained popularity over the last few years, notably because it offers the possibility to correct errors in the evaluation of the macroscopic strain and to non-invasively map local strains (Evans and Holt, 2009; Ní Annaidh et al., 2012; Xu et al., 2019). Due to large variations in mechanical properties and the nonlinear elasticity of skin, there is considerable difficulty in converting strains to stresses for the calculation of the J-integral. Nevertheless, the local strain maps that can be obtained from DIC provide valuable information on the distribution of strains, and especially their concentration near the tip of a crack, and the size of the processing zone (where a high strain gradient can be observed). Potentially, strain-based criteria for failure could be evaluated. Changes in shape of the tear opening can also be observed. Liu et al. (Mincong Liu et al., 2019) performed this analysis on a PVA dual-crosslink hydrogel, and observed a steady-state propagation of the crack, meaning that, once initiated, it propagates in a self-similar manner if one follows the position of the crack tip. They also noted that prior to propagation, the strain level in the static blunted crack is higher.

The present study aims to provide a quantitative analysis of the toughness of porcine skin, by adapting conventional testing techniques to this material. Methods to estimate toughness in Mode I and Mode III are presented. Strain profiles from the crack tip of pre-notched skin SENT samples are measured using digital image correlation, showing the evolution of strains near a crack. Effects of sample orientation and initial crack size are discussed. Moreover, microstructural effects associated with tear mitigation in skin are further characterized with a systematic microscopic analysis of the arrangement of collagen fibers: first *ex situ* transmission electron microscopy (TEM), and then *in situ* environmental scanning electron microscopy (ESEM), coupled with a micromechanical tensile testing device.

2. Methods and materials

2.1. Sample extraction and preparation

Pig skin samples were obtained from two juvenile (~9 weeks old) piglets, provided from the Veterinary School at the University of Cambridge. Removal of the skin was done within a few hours after sacrificing. To facilitate the tracking of displacements on the surface of the skin, the epidermis was depilated using a commercially available hair removal cream (Veet, Reckitt Benckiser Group plc, Slough, UK). Excess fat on the proximal side of the skin was removed with a surgical scalpel. Samples were extracted following two distinct orientations, i.e. parallel (longitudinal sample) and perpendicular (transverse sample) to the direction of the spine. For trouser and crack opening tests, rectangular sections of 80 mm × 25 mm and 60 mm × 50 mm were cut, respectively. All samples were extracted from the same piglet. For SENT tests, a dumbbell-shaped cutting die was used to extract the samples from the second pig; the exact dimensions are further detailed below. Lastly, smaller rectangular sections of approximately 40 mm × 10 mm were isolated for *in situ* testing in the ESEM. Prior to testing, the dimensions of each sample were remeasured to account for effects of tissue expansion or shrinkage. Every sample thickness was measured in three equally distant locations across the length of the sample (in the middle, and ~1 cm away from each side) using a digital caliper with a resolution of 0.01 mm. The measured values were subsequently averaged. All samples were kept in mildly hydrated plastic bags and stored in a cold room at 4 °C. Mechanical testing was performed within 2 days post extraction. Due to the relatively short duration of each test, no particular precaution was taken to ensure sample hydration during testing.

2.2. Experimental methods

2.2.1. Tensile testing setup

A conventional tensile testing machine (HTE Hounsfield) was used to perform the mechanical tests, with a 5 kN load cell. During testing, a crosshead speed of 0.3 mm/s was applied, and the load-displacement curves were recorded. Additional specifications for each experiment are detailed in the sections below.

2.2.2. Trouser test samples

The trouser test, used for rat skin by Purslow (1989) and porcine dermis by Comley and Fleck (2010), is a well-established method used to determine the fracture toughness of elastomeric materials in the tear mode (Rivlin and Thomas, 1953). A rectangular sample is cut centrally along its length so that two legs are formed. The legs are pulled in opposite directions, and the force at which the cut starts growing is measured (Sawyers and Rivlin, 1974). Fig. 1a provides the trouser sample dimensions that were used for the present study. The hatched area designates the portion of the sample that is attached to the grips. Specifically designed grips were used, to reduce the likelihood of slippage during testing, as explained in (Pissarenko et al., 2019). Samples are cut with a sharp razor blade in the middle along their length, forming legs with a length of 50 mm, which corresponds to an effective pre-crack length of 25 mm excluding the gripped parts. The intact portion of the sample, along which the crack propagates during the test, has a length of ~30 mm. Fig. 1b shows a real trouser sample of pig skin, which is subsequently mounted on the testing machine, as shown in Fig. 1c. Samples are mounted loosely so that no load is applied on the skin in the beginning of the test, i.e. the initial distance between the two grips is much smaller than double the effective leg length of the sample. The load cell is then zeroed. During testing, the legs of the trouser sample are gradually pulled apart such that the tissue is undergoing Mode III shear. This was done until complete failure, i.e. the separation of both legs. Three longitudinal and three transverse samples, taken from the same pig, were tested.

2.2.3. Crack opening tests

As mentioned earlier, Yang et al. (2019) designed a set of grips to perform Mode I crack opening tests on arapaima scales. The same methodology was applied here for pig skin, and the dimensions of the samples were adapted to fit the gripping area, indicated by the hatched region on Fig. 2a. A pre-cut was made along the length of the sample, starting from the middle of one side, with a length of ~25 mm. Fig. 2b shows a pig skin sample mounted on the testing machine. Note that each grip is connected to the testing machine via pins, enabling free rotation during extension. The initial distance between the grips is set approximately to the side length of the sample (~50 mm as shown in Fig. 2a), so that the skin does not undergo any load before testing, at which point the load cell is zeroed. The effective portion of the sample, along which the crack is meant to propagate during testing, was maintained between two plexiglass plates separated by a thickness ~0.1–0.2 mm larger than the sample thickness, ensuring that the sample stays fairly flat and enabling the visualization of tear propagation, which occurs outside of the plated area (see Fig. 2b). It was assumed that the effect of these plates on the deformation process is negligible, as no notable effect of friction with the plates was observed. No contact pressure was applied between the skin and the plates, hence only adhesion forces would contribute to friction. Samples were still fairly hydrated during testing, and the remaining skin fat and oils also contribute to lubrication of the interface. As in the trouser test, both legs were gradually separated until complete failure of the skin. As the legs separate and the tear propagates across the specimen, the effective portion of the sample progressively leaves the plated area, and the surface in contact with the plexiglass decreases, thus diminishing the effect of friction in the propagation plateau phase. Three longitudinal and four transverse samples were tested, all from the same pig as for trouser tests.

### 2.2.4. Single edge notch tension (SENT) tests

2.2.4.1. Sample mounting and mechanical testing.
Fig. 3a indicates the dimensions of the SENT samples that were obtained after extraction with the cutting die. The resulting gage dimensions are 30 mm × 10 mm. At mid-length of the sample, a pre-notch of length a was made on the side, such that $a/W = 0.25$ (for one longitudinal and three transverse samples), and $a/W = 0.5$ (for 3 longitudinal and 3 transverse samples), where a is the initial pre-crack length and W is the width of the sample. Fig. 3b shows a real SENT sample of pig skin, presenting some slight changes in dimension following extraction. As a consequence, the value of a is adapted to the actual measured width of each sample. Specimens were mounted on the tensile testing machine using the same grips that were used for trouser tests, for an initial grip-to-grip distance smaller than the gage length. The extension was gradually increased at a crosshead speed of 0.01 mm/s, until the load sensor would output a threshold force of ~0.04 N (slightly above the resolution of the load cell), and the skin sample would stay flat. In this reference configuration, the extension sensor was then zeroed and uniaxial tension was applied until complete failure of the tissue. Fig. 3b also shows that a random speckle pattern was applied to the surface of the skin, which was done using a thin permanent marker. The speckle pattern facilitates the tracking of displacements for the DIC algorithm. Each SENT test was
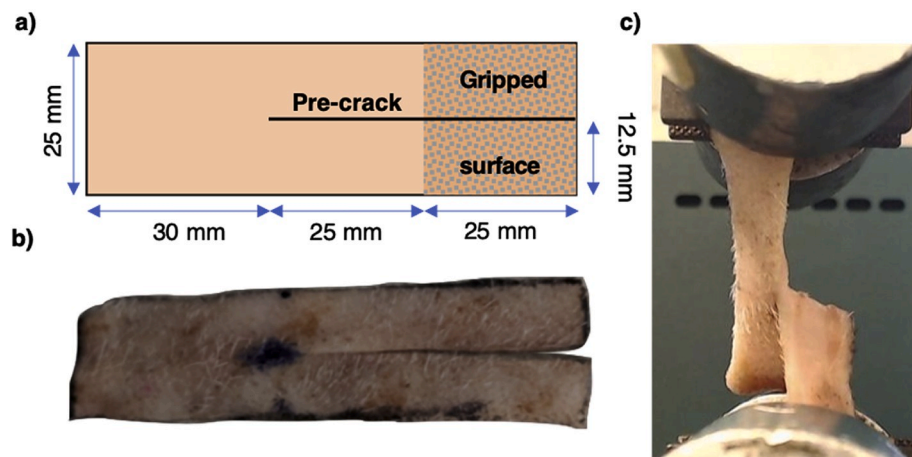
Fig. 1. Trouser tests. a) Schematic presentation of the geometry of a sample. b) Pig skin sample prior to testing, following the dimensions in a (picture scales with a)). c) The sample mounted on the tensile testing machine; the separation of the grips leads to the propagation of the pre-crack.
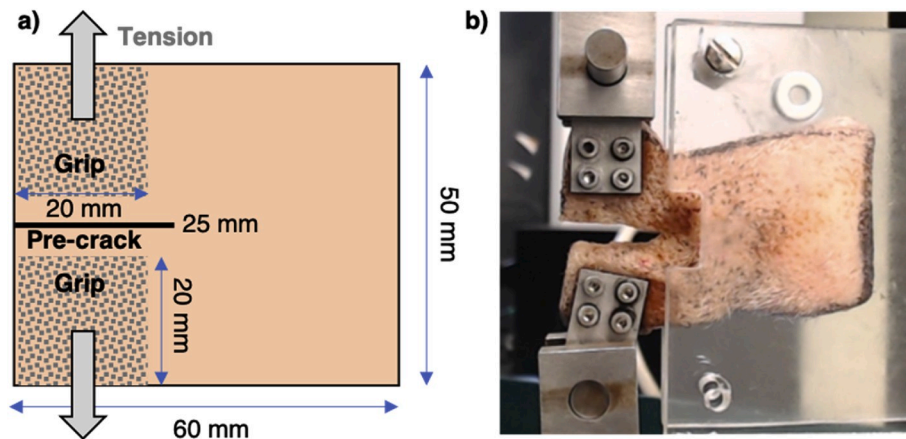
Fig. 2. Sample preparation for crack opening tests. a) Schematic illustration with principal dimensions and testing conditions. b) Pig skin sample prior to testing, mounted with the special grip fixtures, which allow for the rotation of the grips during the opening of the legs. Two plexiglass sheets maintain the sample in-plane during the test, to facilitate image recording and monitor the tear opening process.
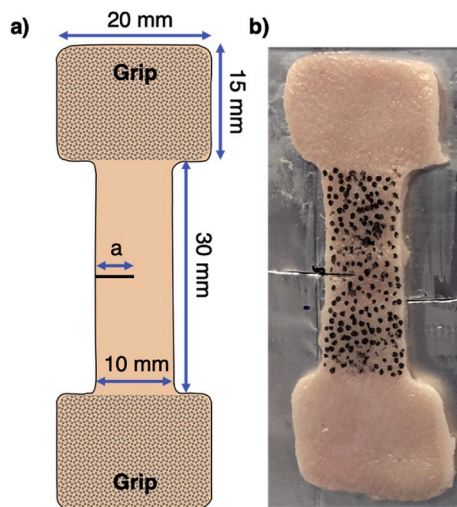
Fig. 3. SENT sample. The specimen is extracted from the skin using a cutting die, with the indicated geometry. a) Schematic illustration of sample, showing the notch on the side, made at mid-length in the gauge region, with length a. b) Pig skin sample, shown for a/W = 0.5. The dimensions of b) scale with a) so that the slight changes in size can be appreciated. The skin is speckled to facilitate post-processing with DIC.

synchronously recorded using a high-resolution camera (Logitech C920), placed in front of the speckled surface. A laser alignment tool was used to ensure that the camera was well aligned with the normal to the sample surface. Placement of the camera in front of the sample yields an average spatial resolution of ~0.12 mm per pixel.

2.2.4.2. Digital image correlation post-processing. The recorded videos from SENT tests were post-treated using the open-source MATLAB software NCorr 2.1 (Blaber et al., 2015). NCorr is particularly suited to track large deformations, as the DIC post-processing algorithm updates the reference image as the sample deforms, in a stepwise fashion. The software provides local measurements of vertical (y-direction) and horizontal (x-direction) displacements and calculates the local Euler-Almansi strains e_{xx}, e_{xy}, e_{yy} in the plane of the image. Key components of the DIC analysis are: a) the subset radius, i.e. the radius in pixels of the circular region used to correlate image subsets; b) the subset spacing defines the spacing in pixels between neighboring subsets. This parameter is further always maintained at 0 as increasing it simply reduces computational load and can introduce inaccuracies in the

measurement of displacements. c) the strain radius sets the size of a planar surface used to compute strains from displacement data by fitting it to the defined plane. Liu et al. (Liu et al., 2019a,b) observed the effects of these parameters on the calculated strains near a crack tip, and discussed the importance of carefully selecting their values in order to obtain a good correlation with a small error. They recommend using values as small as possible for the subset radius and the strain radius, without introducing additional noise or making subset correlation impossible.

Following these guidelines, the accuracy of the measurement of local strains along a transverse line starting from the tip of the notch to the other edge of the sample was evaluated using vinyl rubber as a reference material. Due to the complex nature of skin and to its high variability in terms of mechanical behavior, a hyperelastic isotropic material of known mechanical properties was selected for DIC parameter calibration. Similar SENT tests were performed with a 3 mm long notch, and results from the DIC analysis were compared to numerical results obtained from a Finite Element Model (FEM) of the same loading configuration. These methods and the effect of DIC parameters are further developed in SI I.

For skin samples, DIC parameters were iteratively selected such that the obtained displacement and strain maps provide a good compromise between accuracy (in terms of resolution/size of the subset radius), and consistency, as points near the crack tend to have a poor correlation if the subset radius is too small. The DIC post-processing algorithm was executed for each tested SENT sample.

2.3. Ex situ transmission electron microscopy

2.3.1. Sample loading and region-specific observations

In order to gain a better understanding of the processes of microstructural rearrangement that occur in skin during a SENT test, three additional transverse specimens were isolated for *ex situ* characterization. All samples were initially pre-notched with a/W = 0.5. A first specimen was kept intact (untested); another one was loaded until initiation of the crack propagation is observed, and finally a last one was tested until complete failure. Deformed samples were immersed in the fixative solution immediately after testing and unmounting from the testing machine. For each specimen, strips located in specific regions with respect to the initial crack tip were extracted (~3 mm × 3 mm), as described in Fig. 4:

- A piece of skin containing the crack tip (blue square in Fig. 4), where a high concentration of stresses can be observed. For the failed
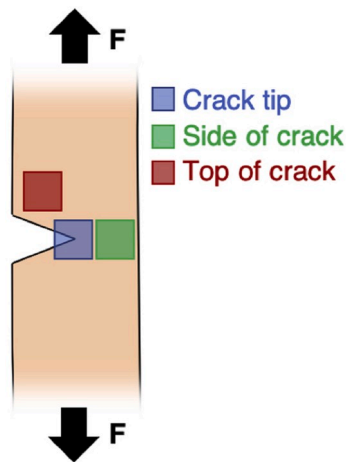
Fig. 4. Schematic illustration of the extracted regions on SENT samples isolated for TEM observation, namely the tip of the crack (blue square), the region on its side, ahead of the crack tip (green square), and the region behind the crack (red square). (For interpretation of the references to colour in this figure legend, the reader is referred to the Web version of this article.)

sample, the areas immediately at the top and at the bottom of the initial crack tip were extracted;

- A piece in the area located on the side of the crack (green square in Fig. 4), which bears most of the uniaxial load during tensile deformation, after the tip of the crack. For the failed sample, this piece was taken slightly above the path of the propagated crack;
- A piece above the notch, well behind the tip of the crack (red square in Fig. 4). During deformation, this area bears almost no load.

2.3.2. Tissue preparation and microscopy imaging

Immediately after extraction, the skin pieces were immersed in a solution containing 2.5% paraformaldehyde, 2.5% glutaraldehyde, and 0.1M cacodylate buffer. The staining and embedding protocol for TEM preparation is detailed elsewhere (Pissarenko et al., 2019). The strips were embedded in low viscosity resin with the hypodermal surface facing the bottom surface of the block. This was done so that sectioning could be more easily performed starting from this side. After trimming ~0.5 mm off the surface of the block, ~70-100 nm thin sections of the dermis were sliced using a Leica Ultracut UCT microtome with a Diatome diamond blade, and subsequently placed on copper grids for TEM observation. A FEI Technai 12 spirit transmission electron microscope was used to visualize the nano-microstructure of skin. To increase the field of observation, grids of images were acquired in areas of interest, i. e. where collagen fibers were principally found. The open-source software IMOD 4.9 (https://bio3d.colorado.edu/imod/) was used to stitch the images together and to correct misalignments.

2.4. In situ scanning electron microscopy of tear propagation

While *ex situ* imaging with TEM provides high magnification visualization of areas of interest at different stages of deformation, *in situ* imaging enables real-time observation of the deformation process. Here, a micromechanical tensile testing device is mounted in the chamber of an environmental scanning electron microscope (FEI XL30 ESEM). The setup is described in more detail in SI II. The skin is mounted with the inner dermal layer facing the objective of the microscope, and the gage dimensions are ~20 mm in length and ~10 mm in width. A side notch of 5 mm is made at mid-length. The sample is then deformed in tension, until failure. Throughout the test, the field of view is adjusted to follow the position of the crack tip.

3. Results and discussion

3.1. Force-displacement curves from trouser and crack opening tests

Fig. 5 provides a summary of the force-displacement curves obtained from trouser and crack opening tests. Both results show similar trends: after an initial nonlinear loading phase, the curve reaches a force plateau, which coincides with crack propagation. Some relative oscillations around the plateau value are observed, until both legs are completely torn apart; the latter corresponds to a sharp drop in applied force. Sample thickness, the calculated average plateau force, and width of the plateau region (the applied extension from propagation to failure) are reported for each sample in Table 1. The force plateau value is generally around ~15 N, and appears to be relatively higher for transverse samples, in particular for crack opening tests. It is also worth mentioning that the extension required to fully separate the legs after crack initiation, i.e. the width of the plateau region, is around ~80 mm, which is significantly larger than the initial propagation length of the samples (~30 mm for trouser tests; ~35 mm for crack opening tests), marking important elastic-plastic deformations occurring in the material during the tests.

3.2. Determination of J_c

Following the methodology of Comley and Fleck (2010) and the equations derived by Purslow (1989) for trouser tests on porcine skin, and earlier fundamental work by Rivlin and Thomas (1953), the toughness J_c of the material is given by:

$$J_c = \frac{2\overline{F}}{t} \tag{1}$$

Where t is the sample thickness, and $\overline{F}$ is the average value of the applied force in the plateau region. The same assumptions are made for opening tests (Mode I). The results for J_{IIIc} (from trouser tests) and J_{Ic} (crack opening tests) are reported in Table 1 for all tested samples. Total averaged values for both types of tests indicate that the overall toughness is generally higher for opening Mode I, with an average of $J_{Ic} = 30.38 \pm 4.90 \ kJ/m^2$, compared to $J_{IIIc} = 20.60 \pm 2.15 \ kJ/m^2$. While differences in orientations are not found for shear Mode III ($J_{IIIc}^{long} = 20.77 \pm 1.11 kJ/m^2$; $J_{IIIc}^{trans} = 20.42 \pm 3.19 kJ/m^2$), more pronounced variations are reported for opening Mode I ($J_{Ic}^{long} = 26.00 \pm 4.41 kJ/m^2$; $J_{Ic}^{trans} = 33.68 \pm 1.13 kJ/m^2$). In the in-plane configuration, the effect of the alignment of collagen fibers (commonly described by the Langer lines) probably plays a more important role. In the transverse orientation, collagen fibers are more likely to be aligned perpendicular to the direction of the crack, and thus more actively mitigate its propagation, reflected here by a higher value of toughness. Out-of-plane deformations probably cause different processes of damage to the collagen network, such as separation and early stage delamination.

Fig. 6 shows the updated Wegst-Ashby modulus-toughness plot (Wegst and Ashby, 2004), with the addition of the values obtained from the present study, for Modes I and III on juvenile pig skin. The average values of the elastic modulus for pig skin were taken from the tangent modulus of the linear region of the deformation curves reported in (Pissarenko et al., 2019). The results for trouser tests fall in the higher range of the previously reported values, and are in good agreement with the values found by Comley and Fleck (2010), who found an average toughness of $J_{cIII} = 17 \pm 4 kJ/m^2$ for porcine skin. On the other hand, the (in-plane) opening mode has a toughness clearly above the range for the skin in the Wegst-Ashby plot, thus extending the quantification of toughness.
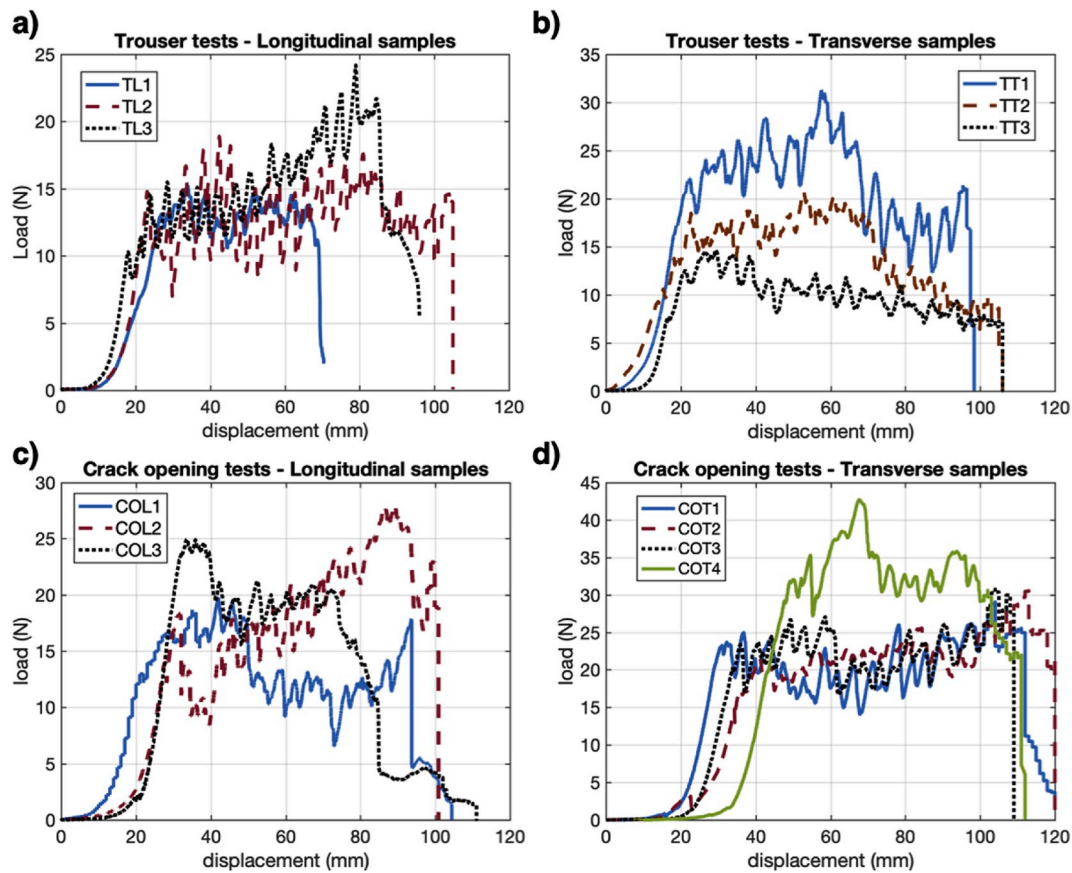
Fig. 5. Load-displacement curves obtained from trouser tests in the a) longitudinal and b) transverse orientations, and from crack opening tests in the c) longitudinal and d) transverse orientations.

Table 1
Summary of experimental results from trouser and crack opening tests. For each sample, the loading orientation and the thickness is indicated, as well as the average force in the plateau region and its width in mm, where legs of the skin samples are separating. The toughness J_c is then calculated from this data and reported in the last column.

Test	Sample	Orientation	Thickness (mm)	Plateau width (mm)	Average plateau force (N)	Toughness J_c (kJ/m^2)
Trouser (Mode III)	TL1	Long.	1.31	42.02	13.09	20.03
	TL2	Long.	1.32	81.3	13.33	20.22
	TL3	Long.	1.44	67	15.88	22.05
	Average Long.			63.44 ± 19.88	14.10 ± 1.55	20.77 ± 1.11
	TT1	Trans.	2.2	75.1	24.16	21.95
	TT2	Trans.	1.53	82.1	17.27	22.56
	TT3	Trans.	1.20	85.2	10.00	16.75
	Average Trans.			80.8 ± 5.17	17.14 ± 7.08	20.42 ± 3.19
	Total Average			72.12 ± 16.10	15.62 ± 4.88	20.60 ± 2.15
Crack Opening (Mode I)	COL1	Long.	1.29	71.7	13.74	21.27
	COL2	Long.	1.39	68.9	18.57	26.72
	COL3	Long.	1.33	52.8	19.94	30.00
	Average Long.			64.47 ± 10.20	17.42 ± 3.26	26.00 ± 4.41
	COT1	Trans.	1.30	80.9	20.92	32.14
	COT2	Trans.	1.30	79.4	22.20	34.27
	COT3	Trans.	1.26	72.7	21.89	34.73
	COT4	Trans.	1.98	61.9	33.16	33.56
	Average Trans.			73.73 ± 8.65	24.54 ± 5.77	33.68 ± 1.13
	Total Average			69.76 ± 9.83	21.49 ± 5.89	30.38 ± 4.90

3.3. DIC analysis of SENT tests

3.3.1. Deformation sequence and crack propagation

The sequence of images in Fig. 7 shows the typical deformation process of tear propagation in a SENT sample of pig skin. After an initial stage of tensile deformation, the tear starts to blunt and stabilizes until a critical deformation is reached in the material, after which the crack rapidly propagates. In the present analysis, particular emphasis is given to the strain state in the tissue shortly before the crack starts propagating.

3.3.2. Evaluation of DIC accuracy on crack tip strain profile

From the DIC post-processing, local Euler-Almansi strains (e_{xx}, e_{xy}, e_{yy}) can be obtained along a transverse line starting from the tip of the
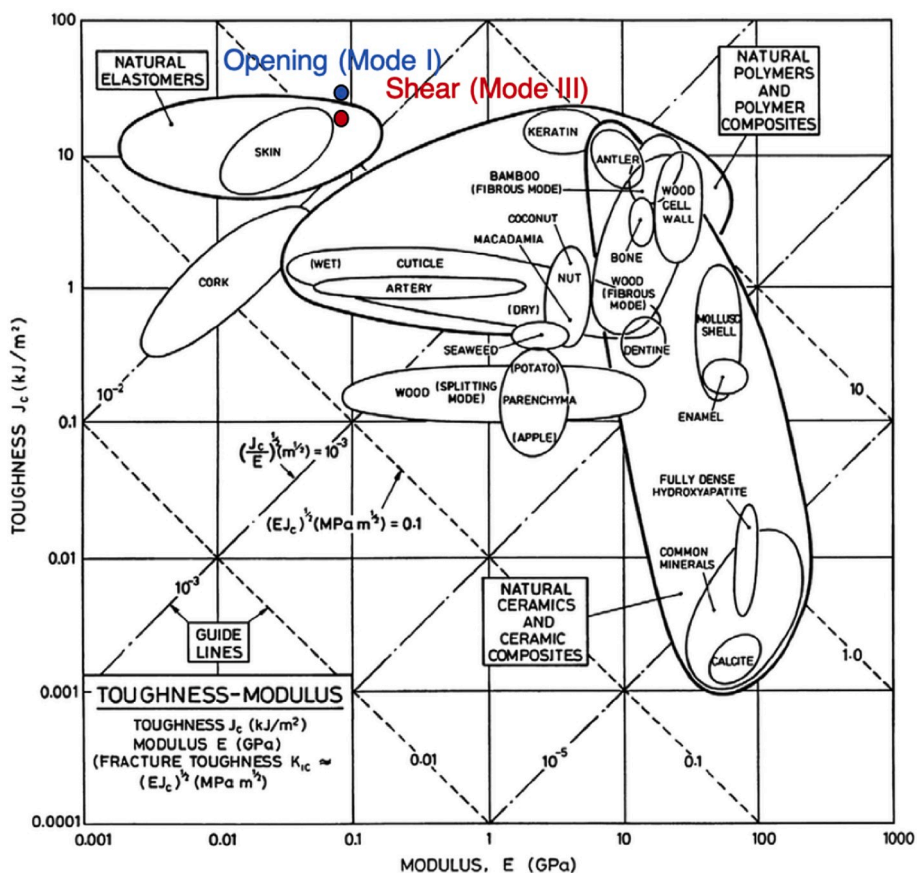
Fig. 6. Updated Wegst-Ashby plot of modulus vs. toughness for several biological materials, including the total average values of J_c estimated in the present work, for trouser tests (red circle) and crack opening tests (blue circle). Circles do not scale with the calculated standard deviations. Reprinted from (Wegst and Ashby, 2004). (For interpretation of the references to colour in this figure legend, the reader is referred to the Web version of this article.)
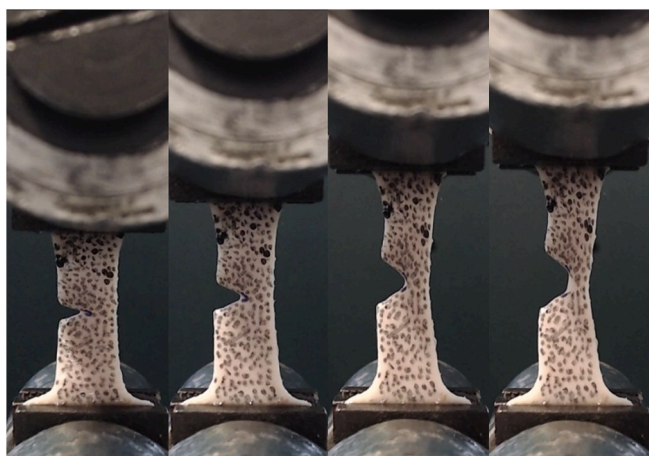

Fig. 7. Time sequence of a SENT test ($a/W \approx 0.5$), shown here for a sample in the transverse orientation. Crack blunting can be observed, followed by tissue delamination shortly prior to failure.

Fig. 8. Crack tip strain profiles before crack propagation on a vinyl rubber SENT sample, obtained by FEM analysis (blue circles) and by DIC analysis of a real sample (red line with crosses), calculated with a subset radius of 10 pixels and a strain radius of 2 pixels. With these parameters, the DIC strain profile most accurately captures the sharp transition in strain close to the crack tip. (For interpretation of the references to colour in this figure legend, the reader is referred to the Web version of this article.)

notch to the side edge of a sample. The comparison between strain profiles obtained from FEM and DIC analyses for a SENT sample of vinyl rubber is presented in Fig. 8. Additional details on the FEM analysis and the DIC parameter optimization are discussed in SI I. The DIC strain profile presented in Fig. 8 (red line with cross markers) corresponds to a subset radius of 10 pixels and a strain radius of 2 pixels, which provided the closest match with the results from FEM analysis (blue circles). Nonetheless, it can be observed that with the present resolution and
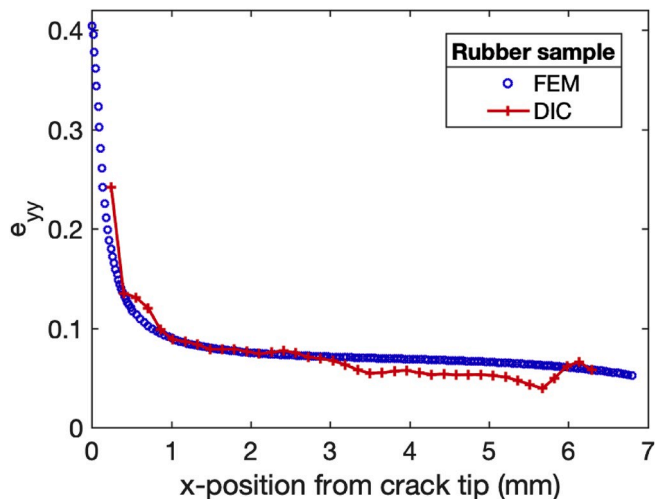
speckle pattern characteristic size, the DIC analysis is not fully able to capture the sharp strain transition in the vicinity of the crack. The maximum value obtained from DIC is about half of the maximum value

obtained via the numerical analysis. It should be pointed out that due to difficulties in tracking deformations exactly at the tip of the crack, measured strains only start approximately 0.25 mm away from the crack tip. After this distance, there is a reasonable agreement between the measured strains and the simulated values, for the selected set of parameters.

3.3.3. Crack tip strain profiles in skin

Fig. 9a–f presents typical 2D strain maps that were calculated from DIC on the same sample at two stages: the blunting phase (Fig. 9a–c) and right before crack propagation (Fig. 9d–f). These correspond to the second and the third images in the sequence in Fig. 7. The maps of e_{yy} (tensile direction, Fig. 9a and d), e_{xy} (Fig. 9b and e), and e_{xx} (lateral direction, Fig. 9c and f) generally show that initially, strains localize around the tip of the crack, in a similar fashion as for standard rubber like materials (see for example SI I.1). Right before the onset of crack propagation, after the notch has blunted, the strains on the surface of the sample become more diffusely distributed. As expected, the region ahead of the crack path bears most of the tensile load (Fig. 9d), and the increased strain level in this area helps to alleviate strain concentration at the singularity, thus delaying the onset of failure at the crack tip. In contrast, the region behind the crack, especially right above the notch, undergoes almost no deformation in the tensile direction. Some lateral stretch shown in Fig. 9c and f can be observed.

Using the strain maps calculated by DIC, one can also plot the strain profile along the crack path. Plots of e_{yy} at different stages of applied extension u_y for different orientations and different initial a/W ratios are presented in Fig. 10 for a set of representative skin samples. For a pre-notch with $a/W = 0.5$ (Fig. 10a and b), the effects of the singularity at

the tip of the crack appear at an early stage of applied extension. In the longitudinal sample (Fig. 10a), a sharp increase in strain can be observed in the vicinity of the crack tip, over a length below 1 mm. Strains in the remaining portion of the crack path stay fairly constant. With applied displacement, the slope near the crack tip gradually increases, and so does the strain level in the constant segment. Besides notable differences in the overall strain level, these strain profiles do not differ much from what can be seen with a standard isotropic rubber like material (see for example Fig. SI I.4 in the Supporting Information). On the other hand, strain profiles in the transverse sample (Fig. 10b), where collagen fibers in the dermis are more likely to be aligned against the path of the crack, follow a different trend. Indeed, the increase in strain is not as pronounced as for the longitudinal sample, and diffused over a larger portion of the crack path, about ~1.5 mm in length. Strains in the remaining segment of the crack path are no longer constant, and instead gradually decrease towards the side edge. Thus, it is likely that fibers in the tissue are progressively recruited, and as a result alleviate the concentration of high strains at the tip of the crack. For a smaller a/W ratio (Fig. 10c and d), strains remain constant in the early stages of deformation. Interestingly, no sharp transition is observed for the longitudinal sample (Fig. 10c), while for the transverse sample (Fig. 10d) the gradient area appears around $u_y = 15.40$ mm, just about ~1.3 mm before propagation of the fracture. At that stage the profiles are quite similar to the ones observed for a longer pre-notch.

At this point, it is not clear whether the strain profile in samples with a low a/W ratio is indeed constant, or if the increase in strain near the tip is very localized and cannot be detected with the resolution available for the present study. Moreover, due to early crack blunting, strains are redistributed along the notch interface and may not necessarily localize
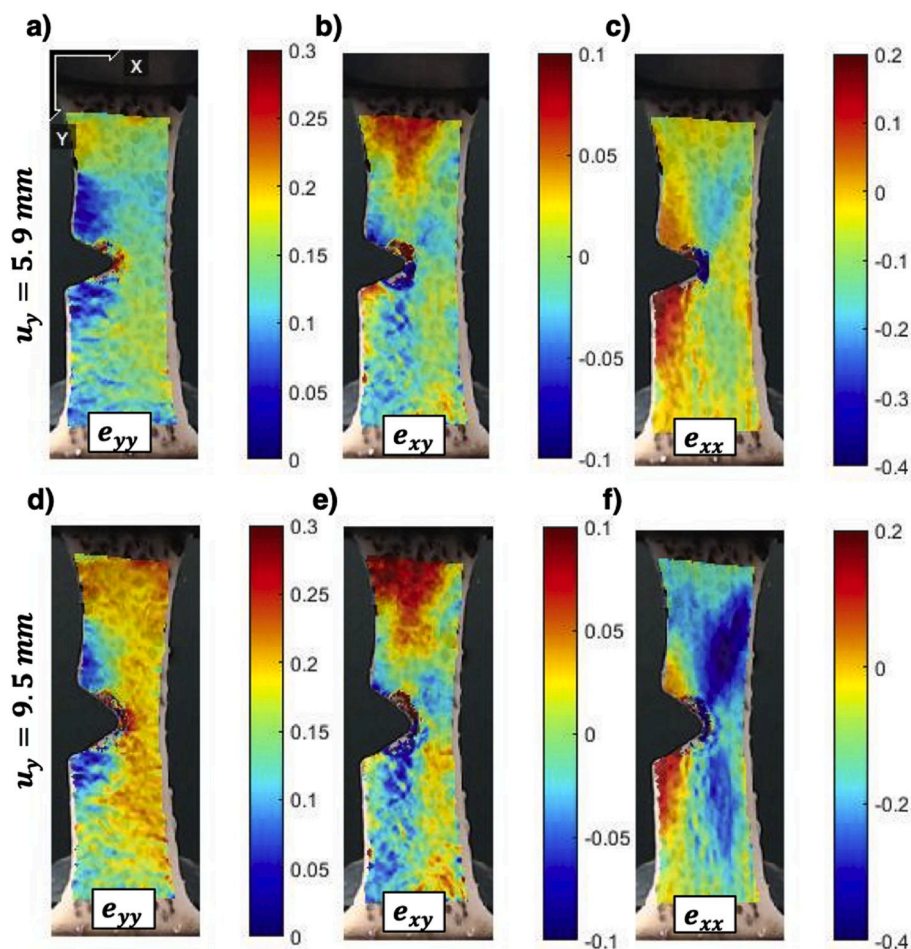

Fig. 9. Strain maps on a transverse SENT sample, calculated by DIC, taken for an applied displacement of $u_y = 5.9$ mm: a) e_{yy}, b) e_{xy}, c) e_{xx}; and for $u_y = 9.5$ mm d) e_{yy}, e) e_{xy}, f) e_{xx}; right before tear propagation. The first row shows that initially, maximum strain values concentrate in a quasi-circular manner around the crack tip. Right before crack propagation (second row), strain distribution appears to be more diffuse, the region on the side ahead of the crack taking up some of the deformation.
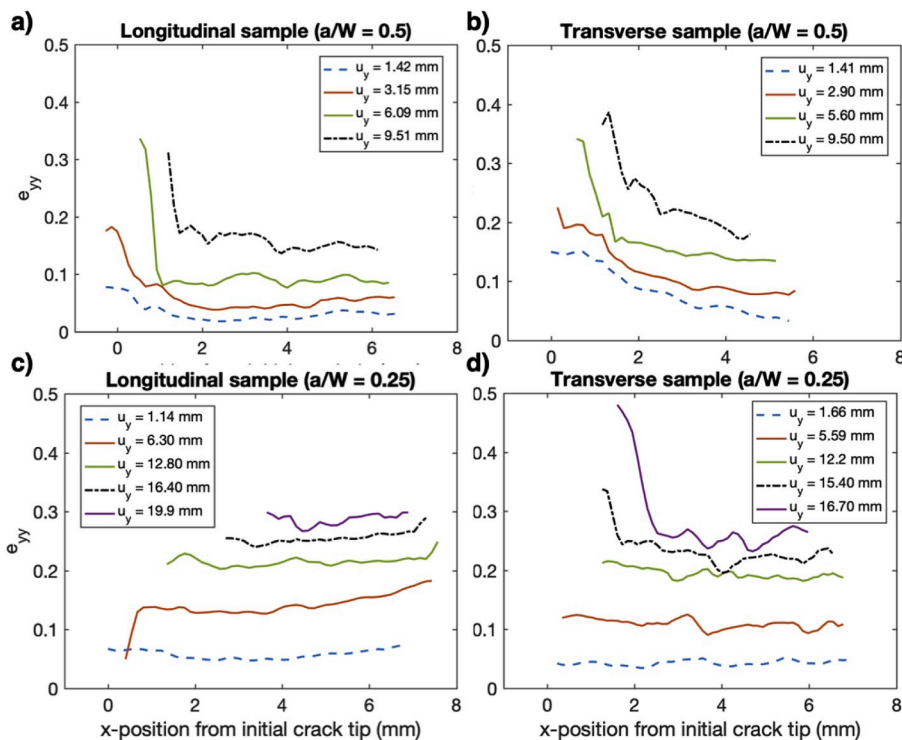
Fig. 10. Crack tip strain profiles along the x-direction from the initial position of the crack tip. Plots of e_{yy} for a) a transverse sample and b) a longitudinal sample for an initial pre-notch with $a/W = 0.5$ are provided at four deformation states, the last state (black dashed line) taking place right before propagation of the crack. Similar plots for $a/W = 0.25$ are shown in c) for a transverse sample and d) for a longitudinal sample at five deformation states, the last state (purple line) is taken before crack propagation. (For interpretation of the references to colour in this figure legend, the reader is referred to the Web version of this article.)

at the exact position of the initial crack tip. To a certain extent, a blunting crack becomes more analogous to a semi-circular edge notch, for which strains are more distributed at the interface, and the maximum strain value along the crack path is significantly lower than for a sharp crack tip (see for example the comparative analysis on both geometries by Liu et al. (Liu et al., 2019a,b)). Local tissue anisotropy may contribute to this effect as well and deflect the path of the crack from the transverse axis. Lastly, some of the tested longitudinal samples failed away from the notched area, suggesting that, at this scale, the notch may not be sufficiently long to induce crack propagation.

It is also revealing to observe the evolution of the maximum strain values, generally found close to the tip of the crack, over the applied extension. These are plotted Fig. 11a and b, for both tested pre-notch lengths and for each sample orientation. The evolution of the maximum strains is quite representative of what is found for the other specimens that were tested. Although differences in the evolution of the strain profile were observed between the two tested orientations, no substantial difference in terms of the maximum e_{yy} value is seen. For $a/W = 0.5$ (Fig. 11a), the large oscillations in $max(e_{yy})$ after $u_y \geq 3.5mm$ correspond to small advances of the crack front. The highest measured strains prior to complete sample failure are 0.413 and 0.406 for the longitudinal and for the transverse sample, respectively. For a shorter pre-notch (Fig. 11b), the evolutions of the maximum strain are more stable and remain at lower values, since no sharp increase near the crack tip appeared on the strain profiles at that stage. This enables further extension of the sample. For the transverse sample, the transition occurs at $u_y = 14.4mm$, after which the maximum value quickly increases until sample failure, at about 0.482. As pointed out earlier, this transition was not observed for the longitudinal sample.

3.3.4. Net-section stress at failure

Because of the uncertainty on the measurement of the maximum strain values, both in terms of accuracy and localization of the singularity, and also because of considerable inter-sample variations, there is not enough evidence to ponder on the influence of orientation or pre-notch size on the maximum e_{yy} value before failure. However, the net-section stress (the applied force divided by the effective cross-section
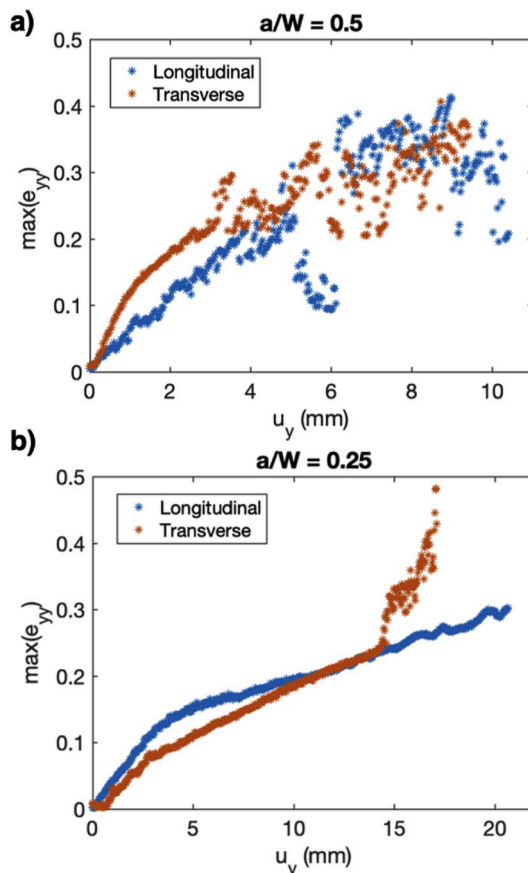

Fig. 11. Evolution of the maximum values of the strain in the tensile direction e_{yy} taken along the crack path as a function of applied extension, plotted for a transverse and a longitudinal sample for a) $a/W = 0.5$ and b) $a/W = 0.25$.

$(W - a)$ of the sample) at which complete failure initiates σ_f can be compared, similarly to what was reported in the work by Taylor et al. (2012) on the toughness of porcine muscle. These values are compiled in Table 2. It should also be noted that average failure stresses of $\sigma_{yl} = 15.31 \pm 3.77$ MPa for longitudinal samples and of $\sigma_{yt} = 19.60 \pm 6.80$ MPa for transverse samples were found from uniaxial tensile tests conducted on the same type of porcine skin, at the applied strain rate of 0.01 s^1, as reported by Pissarenko et al. (2019). To ease the comparison, these results are also reproduced in Fig. 12. Although there is no sufficient data to significantly infer the effect of orientation, transverse samples seem to fail at a higher stress level. It appears that with increasing notch size ratio, the net-section stress at failure decreases. As such, calculated values of the net-section stress at failure are considerably below the measured strength of the tissue, especially for $a/W = 0.5$. Thus, we interpret that crack size has an effect on the strength of the tissue. However, this observation is limited to the two size ratios that were used and to the sample geometry that was used in this study, i.e. crack lengths of ~2.5 mm and ~5 mm for a width of ~10 mm.

In contrast, Taylor et al. (2012) discuss on the high defect tolerance of soft tissues, in the sense that long cracks (from 5 mm to 15 mm in length) do not seem to affect the net-section failure stress of the material. For a fibrous tissue in which fibers are highly aligned along a preferred direction, and if the bonding between these fibers is relatively weak, shear stresses are not transmitted between adjacent fibers and no stress concentration at the crack tip occurs. This is not exactly the case for skin, where collagen fibers in the dermis form a densely entangled network (Pissarenko et al., 2019), probably explaining the observed decrease in net-section failure stress. Moreover, fiber realignment during tension in skin causes rearrangements in the structure which may also play a role in the mitigation of crack propagation, while irreversibly affecting the tissue structure.

3.4. Structural rearrangements of the collagen network

3.4.1. Transmission electron microscopy

A montage of the images acquired by *ex situ* TEM is presented in Fig. 13. Each row corresponds to a specific region, as described in Section 2.3.1, and each column corresponds to a deformation state, i.e. untested, onset of crack propagation, and failure. For the untested configuration, the characteristic tridimensional collagen network is seen. Fibers do not appear to follow any preferential arrangement, perhaps with the exception of the crack tip region, where a certain degree of vertical alignment can be seen. This could either be due to sample or location-related differences, or a consequence of the pre-notch, causing fibers that are not perpendicularly aligned with the direction of the cut to recoil. At the onset of crack propagation, fibers around the tip of the crack are less organized and more compact, and principally lie in-plane. Given that the largest strains concentrate in this region, it is likely that the fiber distribution that is observed is the consequence of tissue relaxation, between the times the sample is

Table 2

Values of the net-section failure stress σ_f, for all the tested SENT samples of pig skin. *Indicates samples for which strain profiles are plotted.

a/W	Orientation	Sample	$\sigma_f (MPa)$
0.5	Longitudinal	L1	6.79
		L2*	6.99
		L3	5.83
	Transverse	T1*	7.90
		T2	7.66
		T3	9.70
0.25	Longitudinal	L4*	9.18
	Transverse	T4	8.34
		T5	15.04
		T6	12.88
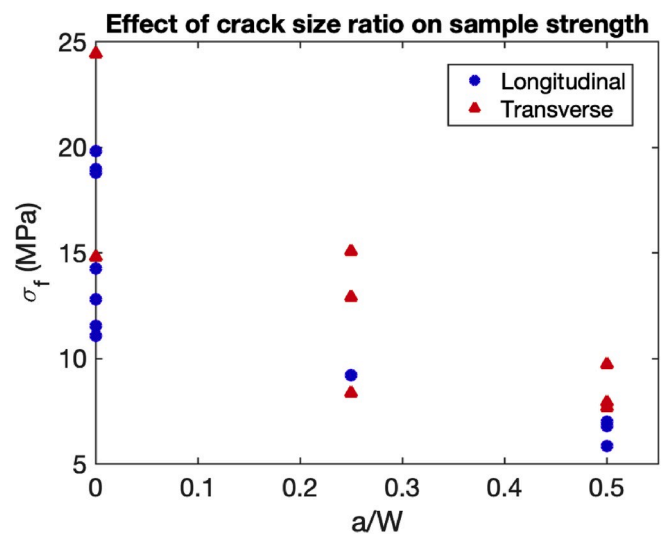
Fig. 12. Effect of the initial crack size ratio a/W on the net-section failure stress, plotted for both observed orientations. Data points for $a/W = 0$ (uniaxial tension) were reproduced from (Pissarenko et al., 2019).

unmounted from the testing machine and the time it is immersed in fixative, or of substantial damage. In the region close to the crack tip, the local strain state is complex: as seen from local strain maps in Fig. 9, it is the area with the maximum levels of shear strain e_{xy} and high compressive transverse strains e_{xx}. On the side of the crack, collagen appears to be highly aligned in the tensile direction. Since the side of the crack is the only portion of the SENT sample that continuously extends from both grips, this region principally alleviates the load from the singularity at the tip of the notch, as seen from the strain maps (Fig. 9d). As also expected from the observed distribution of strains, the structure of collagen at the top part behind the crack is unaltered, the collagen network is dense and highly entangled. Lastly, the post fracture structure of collagen is dramatically changed. In the vicinity of the crack path, loose, out of plane collagen fibrils are observed. This a consequence of the irreversible processes that are fiber sliding, delamination, and ultimately fracture. Right above the crack propagation path, after collagen fibers have undergone realignment and a high level of stretch, fractured collagen fibers recoiled, as seen by the rugged surface of the fibers, which is another indication of considerable damage that has taken place in the structure, except that a higher level of fiber integrity is maintained. Besides a slightly higher degree of fiber alignment, which could be specific to the observed section, no dramatic changes to the structure are seen behind the crack path.

3.4.2. In situ environmental SEM

A notable difficulty in observing the rearrangement of collagen fibers in the ESEM method implemented in this study resides in the fact that the inner layer that is observed still contains a fair amount of subcutaneous fat, and therefore poses a challenge for immediate observation of the collagen fibers in the dermis. Nonetheless, after a certain deformation level, tissue delamination reveals the collagen fibers that contribute to tear mitigation. The sequence in Fig. 14 illustrates this effect, showing that as the sample is deformed, substantial delamination occurs, seen by the progressive appearance of collagen fibers and the erosion of superficial layers. Tear propagation is mitigated by highly aligned extended collagen fibers that bridge the crack, until they reach failure. This is also accompanied by gradual recruitment of the fibers on the side of the crack, which, as discussed above, helps to alleviate the loads near the singularity. This process is illustrated in the schematic sequence of Fig. 15: the initially wavy distributed collagen fibers (Fig. 15a) are gradually recruited in the tensile direction and start straightening, an effect that is more pronounced closer to the crack tip.
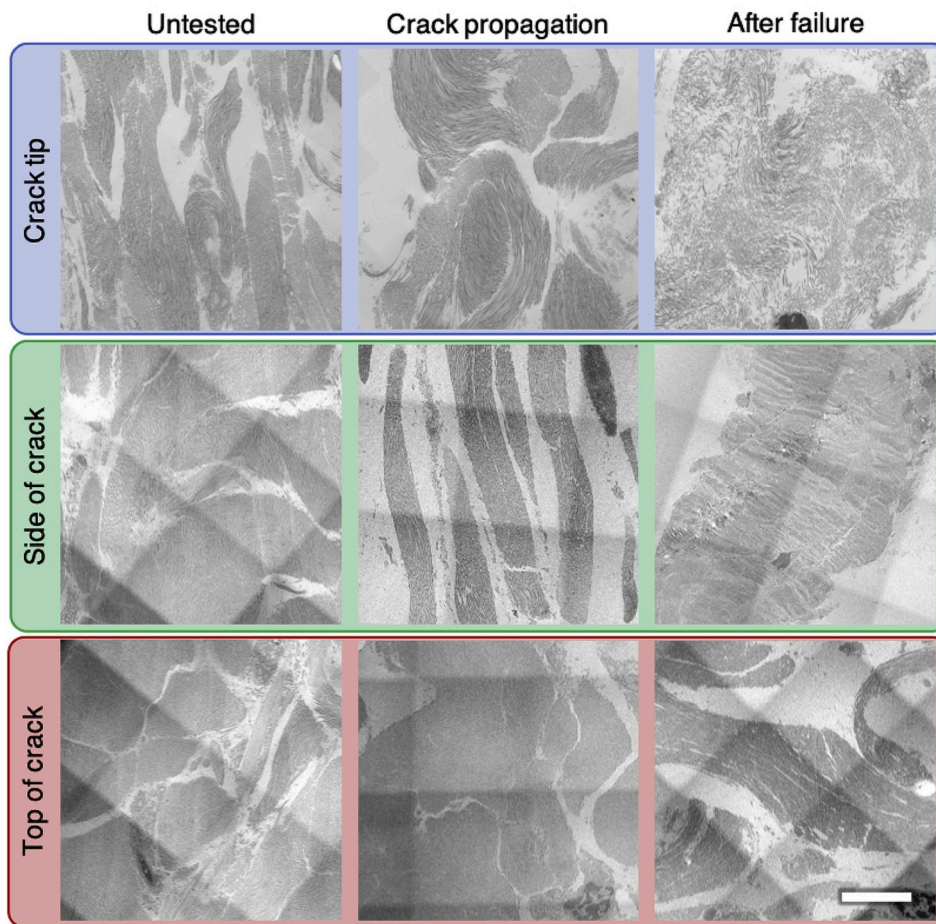
Fig. 13. Stitched TEM images of the three isolated regions of SENT samples of pig skin (Crack tip, side, and top) at three different stages of deformation: untested (first column), loaded until onset of crack propagation (second column), and after tissue failure (third column). The microscopy reveals the arrangement of the collagen fibers for each deformation state, showing regions that underwent the most important changes. Square grids are the result of the stitching process. Scale bar in the bottom right corner = 5 μm (applies to all images).
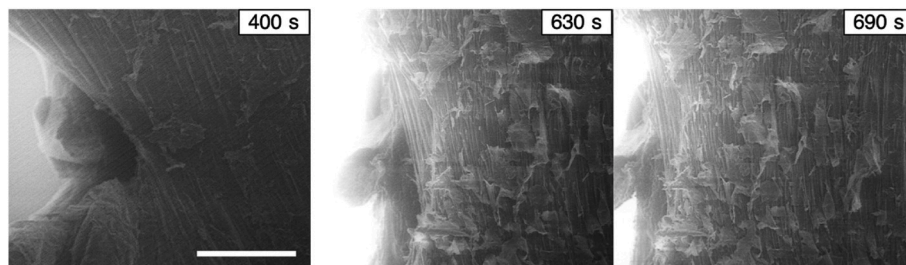
Fig. 14. *In situ* environmental SEM sequence of a pre-notched sample undergoing tensile deformation. The highly extended collagen fibers that bridge the crack tip can be distinguished from the second image, and progressive layer delamination is also observed.

This leads to crack blunting (Fig. 15b). During crack propagation, straightened collagen fibers near the crack bridge the crack and progressively fail, as other aligned fibers ahead of the crack tip mitigate the propagation (Fig. 15c). The recording presented in SI II also shows the progressive delamination of the dermis, accompanied by failure of the stretched collagen fibers.

The post-failure structure of the collagen fibers is further manifested in the series of images in Fig. 16.

4. Conclusions

In the present work, the tear resistance of skin was studied using different approaches, with the aim to provide quantitative estimates for the prediction of tissue failure, and to extend our understanding of the structural processes occurring in the porcine skin that participate to crack mitigation. The principal findings in this study are:

- The toughness was evaluated by conducting out-of-plane tear propagation (Mode III) and in-plane crack opening (Mode I). Average toughness values of $J_{Ic}^{long} \approx 26 kJ/m^2$ and $J_{Ic}^{trans} \approx 34 kJ/m^2$ were found in Mode I, with notable differences between longitudinal and transverse orientations. For Mode III, $J_{IIIc}^{long} \approx 21 kJ/m^2$ and $J_{IIIc}^{trans} \approx 20 kJ/m^2$, suggesting little dependence on sample orientation.
- During tensile deformation of a side edge notched skin sample, strain localization around the tip of the notch is mitigated by blunting of the crack front. Concurrently, the region on the side of the crack reduces high strain concentration by gradual recruitment of the collagen fibers.
- This effect is further exhibited by plotting the crack tip strain profiles during deformation. For a notch size ratio $a/W = 0.5$, the sharp transition in strain near the crack tip is accompanied by a considerable increase of the strains in the remaining segment along the
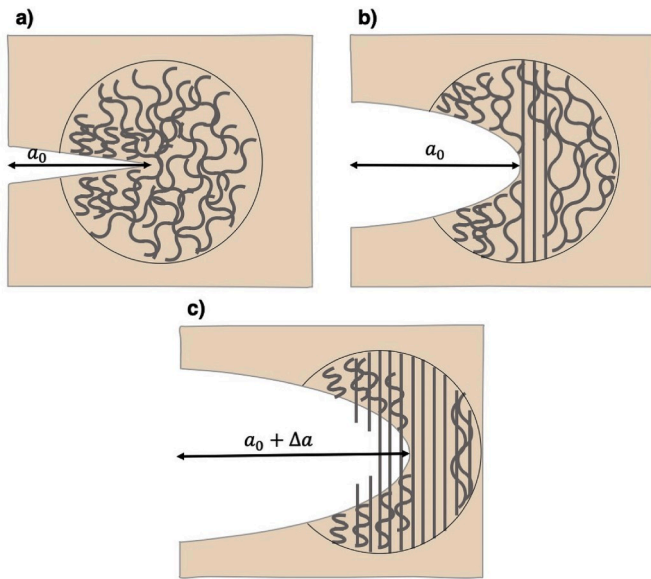
Fig. 15. Schematic illustration of collagen reorganization during the deformation of a pre-notched sample of length a_0.

a) In the initial configuration, collagen fibers are wavy and dispersed. Cut fibers near the notch recoil. b

) During deformation, fibers gradually align in the direction of tension, causing the crack to blunt. Near the crack tip, fibers appear to be more highly stretched. c

) When failure is initiated, straightened fibers bridge the crack until failure. Straight, aligned fibers ahead of the crack tip mitigate crack propagation by alleviating the concentration of stresses near the tip.

crack path, thus reducing the differences between the maximum and the minimum (constant) strain levels in the area. In transverse samples, the strain gradient is reduced and acts on a larger portion of the crack path, suggesting that collagen fibers on the side of the crack contribute to alleviating strain concentration at the tip. For $a/W = 0.25$, localization effects are delayed due to earlier blunting of the notch.

- No notable differences in the maximum strain values before failure are observed in tested orientations. For the same applied displacement, the maximum strain value is notably lower for a shorter prenotch, which delays the onset of failure propagation. More accurate estimates of the strain distribution, and particularly of the maximum strain level prior to tissue failure near the crack tip could be obtained with a finer resolution for DIC.

- Calculated values of the net-section failure stress indicate a considerable effect of pre-notch size ratio when compared to the tissue strength. Even though this observation could be specific to the sample geometry implemented in this study and should be further quantified, results imply that the defect tolerance in porcine skin is quite small ($\leq 2.5\ mm$) compared to other fibrous tissues ($\geq 6\ mm$ for porcine muscle ((Taylor et al., 2012), and $\geq 15\ mm$ for cooked meat (Purslow, 1985))). We attribute this difference to the highly entangled nature of the collagen network in skin, unlike the highly anisotropic arrangement that can be found in muscle. Hence, the pre-notch lengths that were used for trouser and crack opening tests are sufficiently large to provide a correct estimate of the toughness J_c.

- The contribution of the collagen network around the crack and ahead of the crack tip is characterized in more detail by *ex situ* TEM observations, showing that collagen fibers locally realign in the direction of principal tension. Post-failure, irreversible damage in the collagen fibers is clearly seen, with fibril delamination, loss of cohesion, and rugged, less regular structures. These processes contribute to mitigating the propagation of the crack. A notable
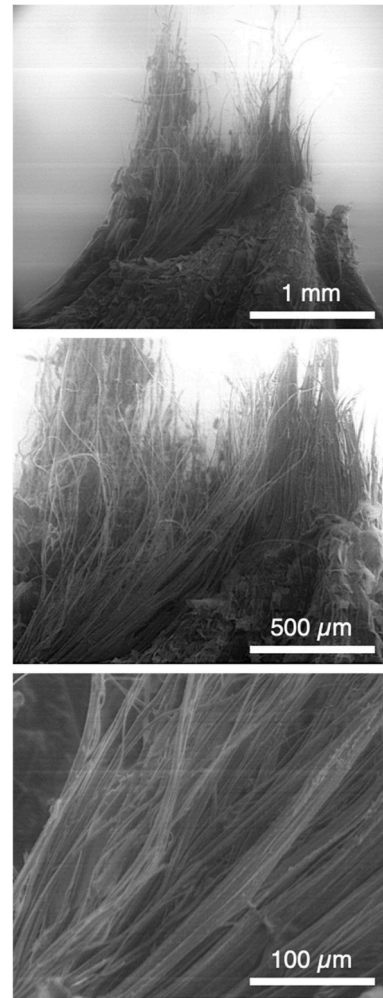
Fig. 16. Post-failure microscopy of a pig skin sample tested in the environmental scanning electron microscope. Close-up visualization of the failed collagen fibers, for which internal damage caused a loss of cohesion, while some of the fibers that had realigned in the tensile direction have recoiled.

limitation of this *ex situ* method stems from the fact that tissue fixation occurs shortly after the sample is deformed and unmounted from the testing machine. In the meantime, the tissue structure has time to rearrange, and therefore the visualized microstructure may not reflect the exact configuration at the moment of deformation. Even so, the method enables high resolution imaging of thin slices of the stained tissue, where irreversible deformations and damage can be seen and long term relaxation processes may have not taken place yet.

- On the other hand, *in situ* environmental SEM provides real-time visualization of the gradual realignment of collagen fibers and gives additional insight into the processes that contribute to the exceptional tear resistance of skin, with crack bridging, progressive delamination, and eventually fracture of the fibers, which recoil after breakage. Although these phenomena were observed in nonphysiological loading conditions (depressurized environmental chamber), it is likely that they also take place *in vivo*, with a more pronounced contribution of the viscous ground substance in the tissue. The method is also limited by difficulties in reaching high resolution and good contrast, and in visualizing collagen rearrangement in the dermis layer. There is therefore a tradeoff between accurately capturing the state of the structure in real-time during deformation *in situ*, and reaching a detailed visualization of the microstructure of the tissue *ex situ*, for samples deformed in

physiological conditions but where structural changes prior to fixation are unknown. The observation of similar features in both methods confirms the important contribution of the dermal collagen fiber network in the mitigation of crack propagation.

Hence, the experimental methods presented in this study can serve as a basis to further establish failure criteria for skin, which, depending on the loading configuration, can find useful applications in domains such as tissue expansion, plastic surgery with reduction of scar zones, and other surgical methods. A relevant example would be the estimate of a critical tensile stretch around an incision of the skin that would not lead to the extension of the cut, in the context of invasive surgery. Results can also apply to the study of stretch marks in skin, which are a consequence of extended stretching over long periods of times, where local delamination and fiber realignment are apparent, a behavior that is akin to crazing in polymers.

Declaration of competing interest

The authors declare that they have no known competing financial interests or personal relationships that could have appeared to influence the work reported in this paper.

Acknowledgements

Appendix A. Supplementary data

Supplementary data to this article can be found online at https://doi. org/10.1016/j.jmbbm.2020.103848.

References

Ankersen, J., Birkbeck, a E., Thomson, R.D., Vanezis, P., 1999. Puncture resistance and tensile strength of skin simulants. Proc. Inst. Mech. Eng. H. 213, 493–501. https://doi.org/10.1243/0954411991535103.

Ashby, M.F., Gibson, L.J., Wegst, U., Olive, R., 1995. The mechanical properties of natural materials. I. Material property charts. Proc. R. Soc. A Math. Phys. Eng. Sci. 450, 123–140. https://doi.org/10.1098/rspa.1995.0075.

Bauer, a M., Russell, a P., Shadwick, R.E., 1989. Mechanical properties and morphological correlates of fragile skin in gekkonid lizards. J. Exp. Biol. 145, 79–102.

Bircher, K., Zündel, M., Pensalfini, M., Ehret, A.E., Mazza, E., 2019. Tear resistance of soft collagenous tissues. Nat. Commun. 10, 1–13. https://doi.org/10.1038/s41467-019-08723-y.

Blaber, J., Adair, B., Antoniou, A., 2015. Ncorr: open-source 2D digital image correlation matlab software. Exp. Mech. 55, 1105–1122. https://doi.org/10.1007/s11340-015-0009-1.

Comley, K., Fleck, N.A., 2010. The toughness of adipose tissue: measurements and physical basis. J. Biomech. 43, 1823–1826. https://doi.org/10.1016/j.jbiomech.2010.02.029.

Evans, S.L., Holt, C.A., 2009. Measuring the mechanical properties of human skin in vivo using digital image correlation and finite element modelling. J. Strain Anal. Eng. Des. 44, 337–345. https://doi.org/10.1243/03093247JSA488.

Hollenstein, M., Ehret, A.E., Itskov, M., Mazza, E., 2011. A novel experimental procedure based on pure shear testing of dermatome-cut samples applied to porcine skin, pp. 651–661. https://doi.org/10.1007/s10237-010-0263-1.

Liu, M., Guo, J., Hui, C.Y., Zehnder, A.T., 2019a. Application of digital image correlation (DIC) to the measurement of strain concentration of a PVA dual-crosslink hydrogel under large deformation. Exp. Mech. 59, 1021–1032. https://doi.org/10.1007/s11340-019-00520-4.

Liu, M., Guo, J., Li, Z., Hui, C.-Y., Zehnder, A.T., 2019b. Crack propagation in a PVA dual-crosslink hydrogel: crack tip fields measured using digital image correlation. Mech. Mater. 138, 103158. https://doi.org/10.1016/j.mechmat.2019.103158.

Ní Annaidh, A., Bruyère, K., Destrade, M., Gilchrist, M.D., Otténio, M., 2012. Characterization of the anisotropic mechanical properties of excised human skin. J. Mech. Behav. Biomed. Mater. 5, 139–148. https://doi.org/10.1016/j.jmbbm.2011.08.016.

Otténio, M., Tran, D., Ní Annaidh, A., Gilchrist, M.D., Bruyère, K., 2015. Strain rate and anisotropy effects on the tensile failure characteristics of human skin. J. Mech. Behav. Biomed. Mater. 41, 241–250. https://doi.org/10.1016/j.jmbbm.2014.10.006.

Pissarenko, A., Meyers, M.A., 2019. The materials science of skin: analysis, characterization, and modeling. Prog. Mater. Sci. https://doi.org/10.1016/j.pmatsci.2019.100634, 100634.

Pissarenko, A., Yang, W., Quan, H., Brown, K.A., Williams, A., Proud, W.G., Meyers, M. A., 2019. Tensile behavior and structural characterization of pig dermis. Acta Biomater. https://doi.org/10.1016/j.actbio.2019.01.023.

Purslow, P.P., 1989. Fracture of non-linear biological materials: some observations from practice relevant to recent theory. J. Phys. D Appl. Phys. 22, 854–856. https://doi.org/10.1088/0022-3727/22/6/026.

Purslow, P.P., 1985. The physical basis of meat texture: observations on the fracture behaviour of cooked bovine. M. Semitendinosus. Meat Sci. 12, 39–60. https://doi.org/10.1016/0309-1740(85)90024-5.

Rivlin, R.S., Thomas, A.G., 1953. Rupture of rubber. I. Characteristic energy for tearing. J. Polym. Sci. 10, 291–318. https://doi.org/10.1002/pol.1953.120100303.

Rodrigues, L., 2001. EEMCO guidance to the in vivo assessment of tensile functional properties of the skin. Skin Pharmacol. Physiol. 14, 52–67. https://doi.org/10.1159/000056334.

Sawyers, K.N., Rivlin, R.S., 1974. The trousers test for rupture. Eng. Fract. Mech. 6, 557–562. https://doi.org/10.1016/0013-7944(74)90012-5.

Taylor, D., O'Mara, N., Ryan, E., Takaza, M., Simms, C., 2012. The fracture toughness of soft tissues. J. Mech. Behav. Biomed. Mater. 6, 139–147. https://doi.org/10.1016/j.jmbbm.2011.09.018.

Vincent, J.F.V., 1990. Structural Biomaterials, Revised ed. Princeton University Press. https://doi.org/10.2307/j.ctt7tbgv.

Wegst, U.G.K., Ashby, M.F., 2004. The mechanical efficiency of natural materials. Philos. Mag. A 84, 2167–2181. https://doi.org/10.1080/14786430410001680935.

Xu, Z., Dela Cruz, J., Fthenakis, C., Saliou, C., 2019. A novel method to measure skin mechanical properties with three-dimensional digital image correlation. Skin Res. Technol. 25, 60–67. https://doi.org/10.1111/srt.12596.

Yang, W., Quan, H., Meyers, M.A., Ritchie, R.O., 2019. Arapaima fish scale: one of the toughest flexible biological materials. SSRN Electron. J. https://doi.org/10.2139/ssrn.3401845.

Yang, W., Sherman, V.R., Gludovatz, B., Schaible, E., Stewart, P., Ritchie, R.O., Meyers, M.A., 2015. On the tear resistance of skin. Nat. Commun. 6, 6649. https://doi.org/10.1038/ncomms7649.